Extreme Convection of the Near-Equatorial Americas, Africa, and Adjoining Oceans as seen by TRMM

MANUEL D. ZULUAGA AND ROBERT A. HOUZE JR.

University of Washington, Seattle, Washington

(Manuscript received 2 April 2014, in final form 3 October 2014)

ABSTRACT

This study documents the preferred location and diurnal cycle of extreme convective storms that occur in the tropical band containing the east Pacific Ocean, Central and South America, the Atlantic Ocean, and northern Africa. Data from the Tropical Rainfall Measuring Mission (TRMM) Precipitation Radar show three types of convective-stratiform structures that constitute extreme convective events: deep convective cores (DCCs), wide convective cores (WCCs), and broad stratiform regions (BSRs). Interim ECMWF Re-Analysis (ERA-Interim) data show the associated synoptic environmental factors associated with the occurrence of extreme convective features. The DCC, WCC, and BSR echoes are associated with early, middle, and late stages of convective system development, respectively, and the statistics and timing of their occurrence are related to topography and life cycle behavior of the convection. Storms containing DCC occur primarily over the Sudanian savannas of Africa and near the mountains in northern South America, being diurnally controlled. Storms with WCC manifest over land, in the same regions as the DCC, but also over oceanic regions. They appear around the clock but with maximum frequency at night. They are favored in regions of midlevel synoptic-scale low pressure systems, which over the sub-Sahara are the troughs of easterly waves. Storms containing BSR maximize over oceanic regions west of Africa and South America, where they exhibit a weak diurnal cycle with a slight midmorning maximum. Off the west coast of South America, the storms with WCC and BSR have longer lifetimes enhanced by orographic lifting over the Andes. The storms with BSR in the east Pacific Ocean often develop into tropical cyclones.

1. Introduction

If Earth had a uniform oceanic surface, its rotation rate and differential of heating between the poles and equator would result in an intertropical convergence zone (ITCZ) encircling the planet at the equator. The near-equatorial Atlantic and Pacific Oceans exhibit trade winds converging in ITCZs that exhibit these characteristics. However, the continents of America and Africa intersect and disrupt these zones. The nature of the interruption by the continents, however, differs markedly. Equatorial Africa is wide, with regions to the east and north comprising vast dry lands. Equatorial America is narrow, with oceanic regions to its north and east and the high Andes mountain range on its western border.

The latitude belt containing these tropical oceans and landmasses corresponds to the region of convective cloudiness that includes various forms of deep convection. An important question in considering the impacts of convection on weather and climate is whether the differing nature of these landmasses intersecting the ITCZ has consequential effects on the structure of the convection. Answering this question is critical to the formulation of accurate general circulation and climate models whose results are sensitive to the feedbacks between convection and the planetary circulation. Many past studies have examined the existence of deep convection in relation to synoptic- and larger-scale circulations. However, up to now, relatively little attention has been paid to the variability of the *forms* taken by extreme convection in the near-equatorial zone, especially that one containing the Atlantic and Pacific ITCZs, and the equatorial landmasses of Central America, South America, and Africa (Fig. 1). Yet this zone contains ocean–land contrasts, sea surface temperature variations, land surfaces ranging from the sub-Saharan zones

Corresponding author address: Manuel D. Zuluaga, Department of Atmospheric Sciences, University of Washington, Box 351640, Seattle, WA 98195.
E-mail: mzuluaga@uw.edu

DOI: 10.1175/MWR-D-14-00109.1

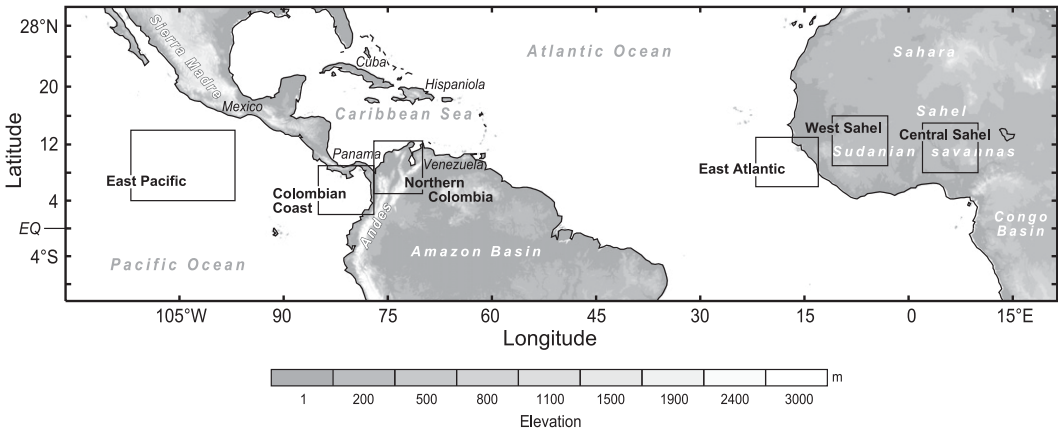

FIG. 1. Geographical regions referred to in this study. The labeled rectangles are regions of composites referred to in the text.

of Africa, and the high mountains of South America. These surface conditions, combined with synoptic and diurnal variability, engender different forms of convection. Since the form taken by convection affects how the convection interacts with the large-scale tropical atmospheric circulation, it is important to understand the varied phenomenology of the convective elements across the region.

Convection in the regions of the equatorial Africa and neighboring eastern Atlantic has been studied many times in the past (Hamilton and Archbold 1945; Houze 1977; Fortune 1980; Houze and Betts 1981; Laing and Fritsch 1993; Thorncroft and Hodges 2001; Fink and Reiner 2003; Schumacher and Houze 2006; Futyan and Del Genio 2007; and many others). Convection over equatorial South America has also been analyzed previously (Betts et al. 1976; Velasco and Fritsch 1987; Garstang et al. 1994; Cifelli et al. 2002), as has convection over the eastern tropical Pacific (Rappaport and Mayfield 1992; Raymond et al. 1998; Serra and Houze 2002). However, none of these studies has examined these regions as a whole, to determine the similarities and differences of convective responses and feedbacks to the large-scale circulation in association with the different underlying land and ocean characteristics. In this study, we employ 15 years of data from the Tropical Rainfall Measuring Mission (TRMM) satellite to examine the convection over this whole near-equatorial zone and to determine the similarities and differences in convective phenomenology across the regions of Africa, South America, and neighboring equatorial oceans.

It is known from past studies of satellite imagery that the landmasses of the tropical Americas and Africa are favored locations for mesoscale convective complexes (MCCs), which include the largest and most intense convective systems (Laing and Fritsch 1997; Nesbitt et al. 2000; Zipser et al. 2006; Liu et al. 2008; Yuan and Houze 2010). These intense or extreme forms taken by convection probably have the greatest impact on the weather, rainfall, and large-scale circulation in this zone. We, therefore, focus here on identifying the more extreme forms taken by the convection seen by TRMM. We document the preferred location and diurnal cycle of the different types of extreme convective storms that occur in this tropical band and, with the aid of reanalysis fields, we identify the large-scale environmental factors (synoptic, topographic, and diurnal) associated with the occurrence of each type of feature.

The TRMM instrumentation (Kummerow et al. 1998, 2000) includes a 2-cm wavelength Precipitation Radar (PR), which has the ability to observe the vertical structure of radar echoes as well as to quantify rainfall rates. The nonsynchronous orbit and near-uniform global coverage of the satellite to observe convection in remote areas in such detail has made it possible to analyze convection without the aid of ground or ocean-based instrumentation and hence to be able to evaluate the behavior of the convective elements across Africa, the Americas, and neighboring oceans. These characteristics make satellite missions such as TRMM and the Global Precipitation Measurement (GPM) mission (Hou et al. 2014) especially useful in the effort to understand severe convection in remote regions of the world with limited observations. The ability of the TRMM PR to see vertical as well as horizontal echo structures allows characterization of the different elements that compose the population of convective clouds. Particularly important is that the detailed spatial resolution of the measurements permits separation of the echoes into convective and stratiform components (Churchill and Houze 1984; Steiner et al. 1995; Houze 1997; Awaka et al. 2009). This subdivision is extremely

useful for distinguishing the nature and organization of the cloud population because it indicates regions with different dynamical and microphysical particle growth mechanisms (Houze 1993, 1997) that lead to a better identification of the most extreme forms of convection in the near-equatorial zone, which is the focus of this study.

The convective-stratiform separation of TRMM PR data have been used by Houze et al. (2007) and Romatschke et al. (2010) to identify extreme echo elements occurring over South Asia, Barnes and Houze (2013) and Zuluaga and Houze (2013) for events occurring over the Indian Ocean and western Pacific, and by Romatschke and Houze (2010) and Rasmussen and Houze (2011) to identify extreme convective events over South America. These studies have related the occurrence of extreme echo cores to the synoptic-scale flow, topography and the diurnal cycle of convective elements in each region to elucidate mechanisms favorable for the occurrence of different forms of extreme convective storms. Those studies have led to better understanding of storms producing severe weather and flooding in those regions (e.g., Rasmussen and Houze 2011; Houze et al. 2011; Rasmussen et al. 2014), and of how the different forms of convection manifest within the different phases of the Madden–Julian oscillation (Barnes and Houze 2013). Different forcing mechanisms (e.g., low-level jets impinging on topographic features, wave disturbances, and diurnal cycle of insolation) acting on environments with pronounced low-level temperature and moisture advection were identified in those studies as key factors favoring the occurrence and the upscale growth of convective systems into larger regions of widespread precipitation (e.g., Medina et al. 2010; Rasmussen and Houze 2011).

The present study will apply similar analysis of the TRMM PR data to the near-equatorial zone encompassing the tropical Americas and Africa in order to achieve a better understanding of extreme convection and its impacts in this region of the world. Section 2 of the paper describes the data and the methodology for identifying extreme echo elements. Section 3 examines the June–July–August (JJA) climatology of winds, divergence and humidity fields, highlighting the key features related to the location of extreme storm systems observed in the region of analysis. Section 4 investigates the spatial distribution of the extreme echo categories defined in section 2, and analyzes the contribution of rainfall, area covered by rain, and lightning flash counts by echo category. Section 5 describes the environmental conditions associated with the occurrence of extreme echo elements, while section 6 analyzes the diurnal variability of the same echo elements. Section 7 lists and discusses the conclusions of the work.

2. Data and methodology

This study uses TRMM 2A25 and 2A23 version 7 datasets that are derived from measurements made with the TRMM Precipitation Radar (Simpson et al. 1988; Kummerow et al. 1998, 2000). Data for JJA for all years from 1998 to 2012 over the domain of interest (10°S–30°N, 130°W–30°E; Fig. 1) were processed following the methodology of Houze et al. (2007) and Romatschke et al. (2010). Rain classification (“stratiform, convective, and other,” Awaka et al. 2009) and attenuation-corrected reflectivity fields (Iguchi et al. 2000, 2009) from the TRMM PR products were remapped onto a latitude–longitude grid with 0.05° × 0.05° horizontal and 0.25-km vertical resolution.

From the interpolated fields, we identify convective and stratiform echoes that develop extreme characteristics of intensity, height, or horizontal extent. For this, we locate 1) deep convective cores (DCC), which are contiguous convective echo volumes with reflectivities greater than 40 dBZ that reach at least 10 km in height; 2) wide convective cores (WCC), which are contiguous convective echoes with reflectivities greater than 40 dBZ and extend over 1000 km^2 when projected on a horizontal plane; and 3) broad stratiform regions (BSR), which are contiguous stratiform echoes (with no reflectivity threshold) that extend over an area of at least 50 000 km^2 when projected onto a horizontal plane. Echo cores that qualify as both DCC and WCC (i.e., both deep and wide) are denoted DWCC.

In this study, we extend the use and identification of these echo object categories to the near-equatorial zone landmasses of Africa and South America. Specifically, we use the above definitions of DCC, WCC, and BSR echo objects, which have been found to be most useful over land. When we have focused on extreme convection over oceanic regions, we have found it necessary to relax the definitions by using a threshold of 30 dBZ instead of 40 dBZ to identify DCC and WCC (Barnes and Houze 2013; Zuluaga and Houze 2013). In the present study, we are largely interested in the behavior of convection over land and its contrast with convection over the immediately adjoining oceans. For this purpose, we have in most instances used the 40-dBZ threshold. However, in analyzing diurnal cycles in section 5 we use the 30-dBZ threshold to bring out the behavior of convective elements over the oceans off the west coasts of Africa and South America.

It is important to note that the DCC, WCC, and BSR are extreme echo objects embedded in larger storms. Therefore, for each of the echo structures described above, the region surrounding each echo core with contiguous reflectivity values greater than zero was also

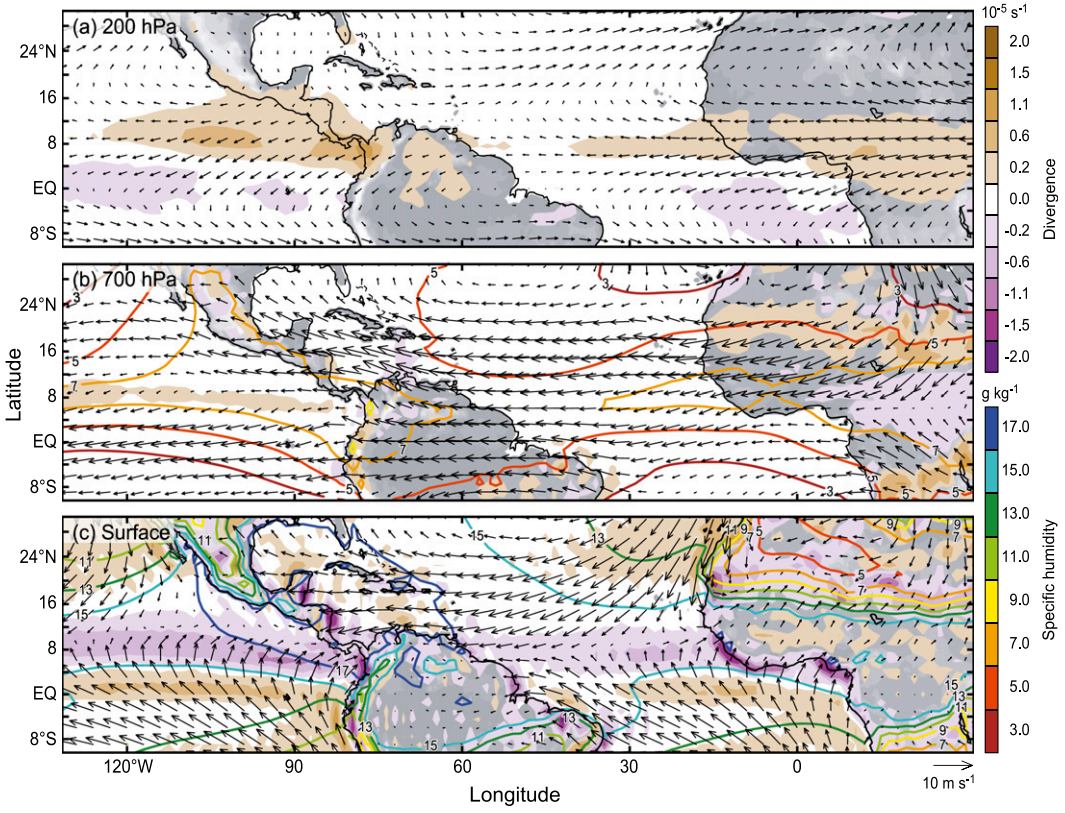

FIG. 2. JJA ERA-Interim climatology of divergence (shading, $10^{-5}\,s^{-1}$), specific humidity (colored contour, $g\,kg^{-1}$), and horizontal wind (vectors, $m\,s^{-1}$) for (a) 200 hPa, (b) 700 hPa, and (c) surface levels for the 1998–2012 period.

identified to locate the full extent of the precipitating system (or "storm") that contained the cores. For each of the identified echo cores and the full echo region containing them, shape parameters such as area, vertical extent, and location of the centroid were calculated. Volumetric rain rate is computed using the near-surface rain product (Iguchi et al. 2009) in the TRMM 2A25 v7 dataset. Lightning flash rate derived from the Lightning Imaging Sensor (LIS; Boccippio et al. 2000; Cecil et al. 2014) is estimated inside the horizontal area projected by each echo element.

Large-scale synoptic conditions over the area of interest are extracted from the Interim European Centre for Medium-Range Weather Forecasts (ECMWF) ReAnalysis (ERA-Interim) data (Berrisford et al. 2009). Three-dimensional 6-h data (horizontal and vertical wind components, geopotential height, and specific humidity) were obtained at 1.5° × 1.5° horizontal resolution, at seven atmospheric levels from 1000 to 200 hPa and for the same TRMM data period used in this study. A composite analysis is used to investigate the environmental conditions associated with each type of extreme echo object identified before. Composite anomalies of each atmospheric field for the time nearest to the occurrence of an extreme echo were computed by subtracting the field at each pressure level from the climatological composite mean incorporating the times of all the extreme events considered in the analysis. Similar composites were constructed for times before and after the occurrence of the event.

3. Climatology of winds, divergence, and specific humidity over the African and American equatorial zones

During JJA, the climatological atmospheric conditions for the equatorial Western Hemisphere are characterized by low- to midlevel quasi-permanent anticyclonic circulation features, which are centered in the subtropics and favor convergence of the northeast trades and the cross-equatorial flow from the Southern Hemisphere (Fig. 2). The farthest northward position of this near-equatorial ITCZ region occurs in the months of JJA favoring rising of air to form clouds and precipitation. To understand the locations and conditions favorable for the occurrence of the most extreme forms of convection, we briefly review

some key features of the climatological setting over the African and American sectors.

Strong baroclinicity between the Saharan region and the vegetated region of central Africa is evident in Fig. 2. The African easterly jet (AEJ; Burpee 1972; Thorncroft and Blackburn 1999) seen as the strong midlevel easterly flow at 700 hPa in central to West Africa in Fig. 2b is largely a product of this baroclinicity. Synoptic-scale African easterly waves (AEWs) form as a result of baroclinic-barotropic instability of the AEJ, and the troughs of these waves, passing every few days, are regions conducive to the formation of strong convection (Burpee 1972; Houze and Betts 1981; Thorncroft and Blackburn 1999). At lower levels, beneath the easterly flow, southwesterly West African monsoon flow brings low-level moisture into continental regions from the Gulf of Guinea (Fig. 2c). The surface conditions depicted in Fig. 2c show sharp convergence of dry northerly and moist southwesterly low-level air along the boundary of these two regions. When AEW troughs pass over this zone, convection breaks out on the monsoon moist side of the boundary. The combination of the warm moist monsoon air at low levels with the midlevel dryness of the AEJ creates a potentially unstable situation. The potential instability is released by synoptic-scale lifting in the wave trough. Several studies have described the synoptic conditions favoring deep convection and precipitation in regions ahead of the AEW trough (Carlson 1969; Burpee 1972; Payne and McGarry 1977; Reed and Jaffe 1981; Fink and Reiner 2003; Guy and Rutledge 2012). The strong wind shear associated with the AEJ combines with the thermal and moisture stratification [as described by Moncrieff (1992)] to favor convection in taking the form of squall lines with trailing stratiform regions and midlevel rear inflows (Smull and Houze 1987). These squall lines frequently occur in the central and west Sudanian savannas, south of the Sahel region (e.g., Aspliden et al. 1976; Fortune 1980; Houze and Betts 1981; Rowell and Milford 1993; Hodges and Thorncroft 1997; Fink and Reiner 2003; Futyan and DelGenio 2007). The structures of these squall line systems have been examined by Schumacher and Houze (2006), Cetrone and Houze (2011), and Powell et al. (2012).

Over the Caribbean Sea and Central America at the surface (Fig. 2c), strong easterly winds form the Intra-Americas low-level jet (IALLJ), a factor considered essential to understanding the climate of the Caribbean region (e.g., Amador et al. 2006). The IALLJ is barotropically unstable, and its variations are related to amplification and weakening of the large-scale circulation of the North Atlantic subtropical high (Amador 2008). Over the Caribbean just north of South America the prevailing surface winds are predominantly easterly. However, over the eastern Pacific, the cross-equatorial flow from the south curves toward the landmass so that a persistent southwesterly flow interacts with the Andes mountain range in western Colombia (around 80°W in Fig. 2c). This low-level warm and moist flow is known as the Chocó jet (Poveda and Mesa 2000; Poveda et al. 2006) and often ascends the topography to interact with a relatively drier midlevel easterly wind to produce a region of surface convergence and upper level divergence (cf. the winds near the Pacific coast of Colombia in Figs. 2a,c). This region is of particular interest because it corresponds to a climatological maximum in rainfall (Mapes et al. 2003), a large concentration of mesoscale convective complexes (Velasco and Fritsch 1987; Zuluaga and Poveda 2004), relatively high sea surface temperature (SST), and low salinity (Alory et al. 2012). The Chocó jet is partially monsoonal, associated with ocean–land heating contrast and convection over the region (Mapes et al. 2003). It is also thermally driven by the SST gradient between the coastal region of Colombia and the Ecuador–Peru cold tongue (Poveda et al. 2006). In comparison to the many studies of convection over equatorial Africa, relatively little is known about the structures of the convective events occurring in this region of the Americas.

4. Characteristics of extreme echo events

a. Spatial distribution

To achieve a better understanding of the characteristics of precipitating systems occurring over the near-equatorial regions of both the Americas and Africa, we first describe the spatial distribution of the echo elements defined in section 2: DCC, WCC, and BSR. Figure 3 shows the probability of the TRMM PR seeing a specific type of extreme echo core anywhere within the near-equatorial belt containing the east Pacific Ocean, Central America, South America, the Atlantic Ocean, and Africa during JJA. The probability is being presented in a 0.5° × 0.5° resolution grid box and has been normalized by the TRMM sampling frequency, following the methodology of Romatschke et al. (2010).

Deep convective cores (Fig. 3a) occur almost exclusively over continental regions, with maximum frequencies over the western slopes of the Sierra Madre range in Mexico, the Caribbean (northeastern) side of the Andes in Colombia, and a broad zone that encompasses the central and west Sudanian savannas, south of the Sahel region. DCC are also observed, but less frequently, in central Florida in the United States, the Caribbean islands of Cuba and Hispaniola, southern Mexico, the west coast of Nicaragua, and a broad zone in

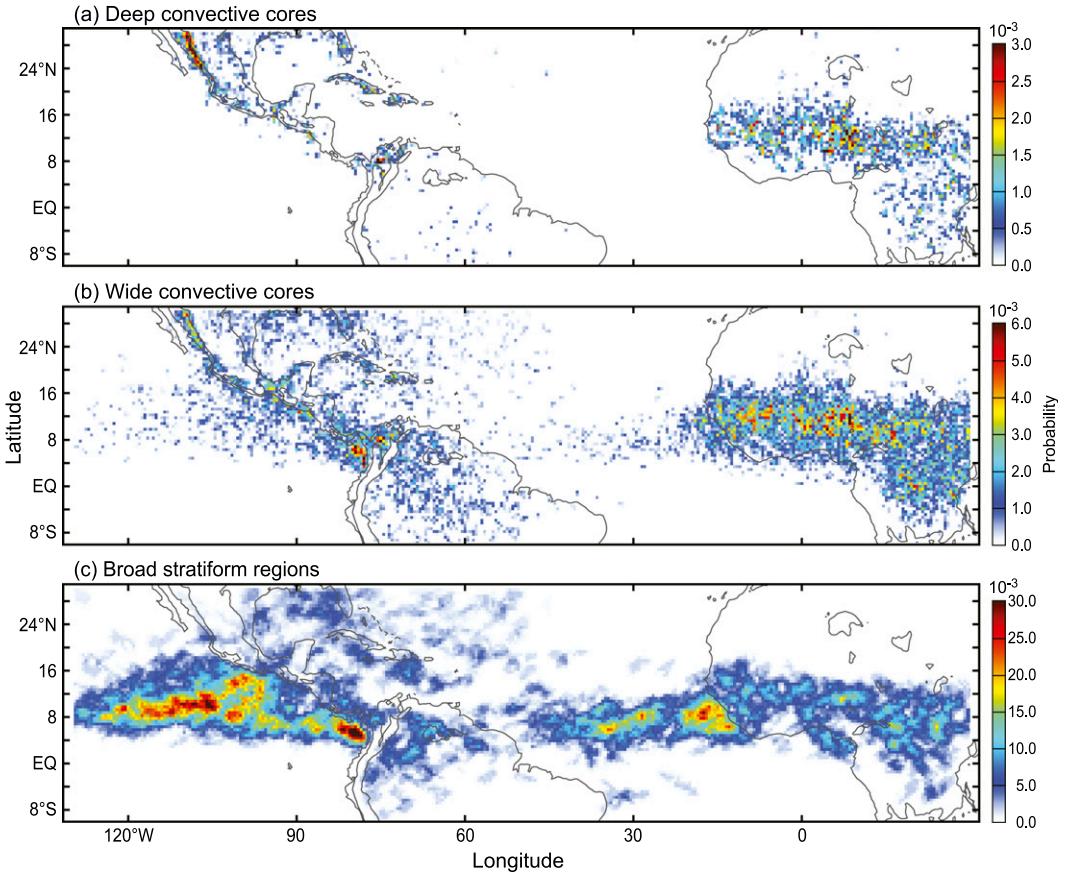

FIG. 3. Spatial distribution of the probability of a location being under (a) a deep convective core, (b) a wide convective core, and (c) a broad stratiform region during the months JJA of 1998–2012. The contour inside the continent represents the 1000-m terrain elevation.

the Congo basin over Africa. DCC are typically characterized as young and vigorous convective cells produced by active strong updrafts that have likely benefited from the peak of low-level buoyancy generated by daytime heating over land. Storms containing DCC have been seen associated with severe weather, flash floods and are more likely to produce lightning (Rasmussen and Houze 2011).

Wide convective cores (Fig. 3b) represent the clustering of intense convective elements to form mesoscale entities; that is, they represent situations in which intense active convective elements have grown upscale to become part of an MCS. Such mesoscale echoes tend to occur in the same regions as the DCC, but they also extend into the surrounding oceans. This category of convective elements generally occurs at a somewhat later time of day than DCC (e.g., Romatschke et al. 2010; Romatschke and Houze 2010). Romatschke and Houze (2010) and Rasmussen and Houze (2011) have further shown that the maximum frequency of occurrence of WCCs occurs downstream of the location of maximum frequency of DCCs. These behaviors indicate statistically that the WCC characterizes a later stage of MCS development. By using a ground-based radar located on an island in the Indian Ocean, Zuluaga and Houze (2013) confirmed that the WCC category is typically related to MCSs in an early and strongly convective stage of their life cycle. Some echoes qualify for both the DCC and WCC categories, but we do not require a WCC to also qualify as a DCC. Indeed we note that WCC often occur over oceanic regions where DCC do not manifest; that is, oceanic convection is not as deep as over land but can nevertheless form mesoscale regions of very heavy rain. Illustrative of this fact is that the maximum occurrence of WCC in the west Pacific sector is over the Colombia and Panama coast where few DCC are located, while over the Sudanian landmass of Africa the WCC echoes coincide with the location of maximum DCC occurrence.

Broad stratiform regions (Fig. 3c) are mostly distributed along the ITCZ region, and near coastal monsoonal flows of the tropical east Pacific and Atlantic Oceans. To

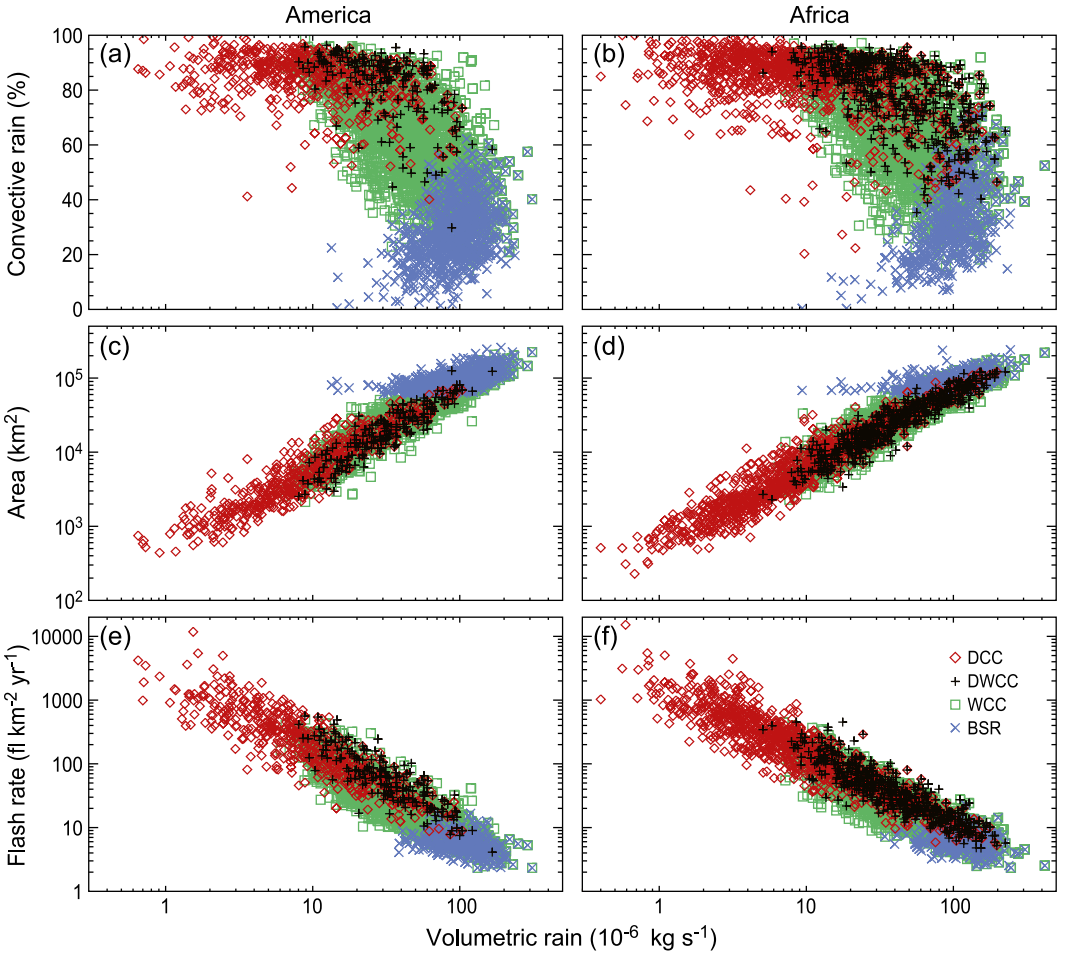

FIG. 4. Scatterplots showing the mass of rain falling per unit time from storms containing echo cores designated as DCC (red), both DCC and WCC (black), WCC (green), and BSR (blue) according to (a),(b) convective rain percentage (%); (c),(d) area of the parent storm (km^2); and (e),(f) lightning flash rate (flashes km^{-2} yr^{-1}).

a lesser extent, they occur over the western slopes of the Andes of Colombia and Venezuela, and over an extended widespread region in the Sudanian savannas of central Africa, extending into the north Congo basin. Zuluaga and Houze (2013) found that the BSR echoes are found most frequently in the late stages of development of MCSs. The regions having the highest probability of occurrence of BSR echoes over the eastern Pacific and Atlantic Oceans are consistent with the results of Schumacher and Houze (2003), who suggested that over oceans MCSs can grow to larger sizes with maximum stratiform coverage because of the nearly unlimited moisture from a relatively warm and humid oceanic boundary layer undergoing only slight diurnal modulation. In contrast, over land, the growth of MCSs and, hence, stratiform rain areas tends to be truncated by nocturnal cooling of the boundary layer unless a moist steady flow is provided by wind shear or a favorable synoptic condition that can maintain a coherent structure through the nighttime. The near-coastal regions of the eastern Pacific and Atlantic are also known to be the favored locations for tropical cyclogenesis, and the patterns in Fig. 3c, therefore, suggest that tropical cyclogenesis results from the further development of MCSs that form large stratiform echo regions.

b. *Rainfall contribution, area, and lightning flash count*

We refer to a single contiguous radar echo as a storm. A storm may contain one or more DCC, WCC, DWCC, or BSR echo cores. Figure 4 contains scatterplots of characteristics of storms containing these echo core types. The characteristics shown are the percentage of convective rain, area covered, and lightning flash rate compared to the total volumetric rain of each of the storms in which the echo elements were embedded. Figure 4 compares characteristics over the American and African sectors (i.e., to the west and the east of 40°W

TABLE 1. Number of events and overall statistics for storms that contain each of the extreme echo-core categories identified in the study. The statistics are stratified to compare characteristics over the American (10°S–30°N, 130°–30°W) and African (10°S–30°N, 30°W–30°E) sectors.

	No. of events		Volumetric rain (10^6 kg s^{-1})		Convective rain (%)		Area (km^2)		Flash rate (flashes km^{-2} yr^{-1})	
	America	Africa	America	Africa	America	Africa	America	Africa	America	Africa
DCC	585	1136	16.7	19.8	84.1	84.0	11 355	13 624	378.6	346.0
DWCC	197	584	39.5	56.0	81.5	78.9	25 486	35 261	90.2	53.2
WCC	2897	3017	58.5	62.2	62.7	65.5	41 752	42 290	32.7	29.9
BSR	935	545	99.1	107.0	27.9	33.0	95 390	93 800	5.8	6.4

in Fig. 3, respectively). Figures 4a,b show that events with DCC have a greater contribution from convective precipitation but they have relatively low volumetric rain accumulations. In contrast, storms that contain BSR have rain accumulations one–two orders of magnitude greater than storms containing DCC, but the convective rain percentage is relatively low. Storms that contain WCC and DWCC are intermediate between DCC and BSR storms in terms of volumetric rain, area covered, and convective rain percentage. Figures 4c,d show that DCC rainy regions produce relatively low volumetric rain accumulations that extend over small areas, while systems containing WCC and BSR cover greater areas, and have higher rainfall accumulations. This relationship is consistent with the well-known fact that the total rain accumulation from systems of various sizes tends to scale with the areal coverage of the precipitating system (e.g., Atlas et al. 1990). Figures 4e,f show further that storms containing DCC have the highest frequency of lightning flashes even though they represent relatively low overall rainfall accumulations. In contrast, BSR tend to produce the largest rainfall accumulations and have comparatively low flash rates. Storms containing WCC and WDCC are intermediate between storms with DCC and BSR with respect to the flash rates they produce.

Figure 4 emphasizes how the three echo categories analyzed in this study effectively characterize and separate the spectrum of extreme storm types that occur in the tropics, in both intensity and areal coverage. The figure further shows that although the African and American regions are affected by different convective forcing mechanisms, the metrics shown in Fig. 4 are similar in the two regions. Thus, we conclude that the population of storms containing each of the extreme echo structures defined in section 2 is representative of different extreme convective classes that have their own characteristics on rainfall type and accumulation, spatial coverage, and lightning occurrence. Storms in each category can be generically similar on the convective and mesoscale structure though they may be triggered by a variety of synoptic, topographic, and diurnal effects. These latter effects determine the location and frequency of occurrence of storm types for different regions, and hence global patterns of extreme convection.

Table 1 shows details of the overall statistics between extreme convective and stratiform events that occur in the African and American sectors. The African region has a greater number of convective echo elements (DCC and WCC combined) than the American sector. On the other hand, more BSR are found over the Americas compared to Africa. The number, the individual storm characteristics of volumetric rain, percent convective rain, and area covered are all somewhat greater over Africa. The greater magnitudes of the mean area and rain accumulation of storms that occur in the African sector were also seen in the full set of echo elements that have reflectivity cores of 40 dBZ or greater (whether or not they were categorized as DCC or WCC). The slightly greater magnitude in the area extent and rain contribution that African convective systems experience is perhaps indicative of the environmental conditions that occur in such sectors. Over Africa, the prevailing synoptic conditions favor the occurrence of squall-line systems that traverse the extensive African savannas (Fortune 1980; Houze and Betts 1981). As such, they are not much affected by high terrain features. In contrast, deep convection over the American portion of the region of study is favored by monsoonal flow with marked diurnal cycles, concentrated near mountain ranges along with a lack of strong synoptic variability. Under these conditions, the diurnal cycle limits the period in which the systems can increase in size (Mapes et al. 2003). Table 1 shows that in contrast to the extreme convective elements, BSR in the American sector are more numerous, contain more stratiform rain, and reach greater sizes. The large ocean expanse and the synoptic influence of the trade wind confluence in the ITCZ appear to be patterns especially favorable for the growth of precipitation systems into storms with large areas of stratiform rain in the American sector. These observations are further confirmed later in sections 5b(2) and 5c of the present manuscript.

TABLE 2. Number of echo structures observed in each of the subregions selected for detailed analysis during the JJA months of the 1998–2012 period.

	East Pacific (4°–14°N, 112°–97°W)	Colombian coast (2°–9°N, 85°–77°W)	Northern Colombia (5°–12°N, 77°–70°W)	East Atlantic (6°–13°N, 20°–13°W)	West Sahel (9°–16°N, 11°–4°W)	Central Sahel (8°–16°N, 2°–10°E)
DCC	0	9	108	18	132	241
WCC	117	255	198	159	300	409
BSR	167	55	12	69	31	31

5. Environmental conditions associated with extreme echo events

Comparing Figs. 2 and 3 points to a connection between the locations of extreme echo events identified in section 4a and regions with significant low-level convergence, upper-level divergence, and strong surface moisture gradients. To investigate the environmental conditions associated with each type of extreme convective systems, we select six regions shown in boxes in Fig. 1, which represent the location of a maximum in the occurrence of one or more types of the radar echo structures defined in section 2. These regions are located over the east Pacific Ocean, along the Colombian coast, in the northern Colombia region (for the equatorial America sector), over the east Atlantic Ocean, west Sahel, and central Sahel (for the equatorial Africa sector). Table 2 shows the boundary limits and the number of echo structures in each of the selected regions. Sensitivity analysis adjusting the size of the boundaries in the defined regions was performed, and the patterns of environmental conditions described below were not significantly altered. In the following subsections we construct composites of the ERA-Interim for times that TRMM detected one of the echo features that we have defined (DCC, WCC, or BSR). The time used in the ERA-Interim 6-hourly time series was the closest hour of each individual DCC, WCC, or BSR TRMM overpass and is shown as hour 0 in the composites. The number of hours used for computing DCC or WCC composites is smaller than the one reported in Table 2 because some TRMM snapshots have several occurrences of the same echo structure type.

a. Extreme convective elements over the equatorial Africa sector

Figure 5 contains composites of 700-hPa wind vectors and geopotential height anomalies for the hour nearest the time when extreme events occurred in the square regions outlined in each figure panel. Figure 5a shows fields for 283 times when WCC occurred in the central Sahel. Similarly, Fig. 5b shows fields for 214 times that WCC were seen over west Sahel. Figure 5c shows composite fields for 68 times that BSR echoes were detected over the east Atlantic region. Each composite shows an anomalous low pressure trough centered slightly to the east of the region where BSR or WCC events were observed (cf. the broken black lines with the location of the boxes in Fig. 5). We use WCC as a proxy for the occurrences of MCSs over land; the development of intense convection into WCC indicates upscale to mesoscale organization. We use BSR over the ocean since they are a better proxy for MCS occurrence there; that is, stratiform regions manifest more strongly over ocean than over land. The location of a region of mesoscale convection (i.e., maxima in WCC or BSR) ahead of a synoptic-scale wave trough is consistent with previous descriptions of AEW disturbances and where convective activity in the form of squall lines is known to be favored (Payne and McGarry 1977; Reed and Jaffe 1981; Fink and Reiner 2003; Schumacher and Houze 2006; Futyan and Del Genio 2007; Cetrone and Houze 2011; Powell et al. 2012; Guy and Rutledge 2012). Although the composites shown in Fig. 5 are made up of independent samples of extreme mesoscale convective events in the three respective regions, the composite synoptic conditions are highly consistent with these extreme events being associated with westward-moving AEWs of the type known to traverse this region. The picture conveyed by Fig. 5 is of synoptic-scale easterly waves moving westward and supporting strong convection taking the form of WCC in the zone of large-scale upward motion ahead of the wave trough.

The region ahead of an AEW trough is known to be characterized by enhanced low-level convergence in a shallow moist layer, which is overridden by a relatively dry layer aloft (Reed et al. 1977). Figure 6a shows longitude–height composites of divergence and zonal–vertical wind for 155 times when DCC echoes occurred in the box located over the central Sahel. Figure 6b shows composite fields for 87 times that DCC occurred over west Sahel, while Fig. 6c shows composite maps for 136 times that WCC echoes were seen by TRMM over the east Atlantic. We use WCC over the ocean region, since DCC are not observed over the ocean. Horizontal and vertical cross sections using WCC instead of DCC

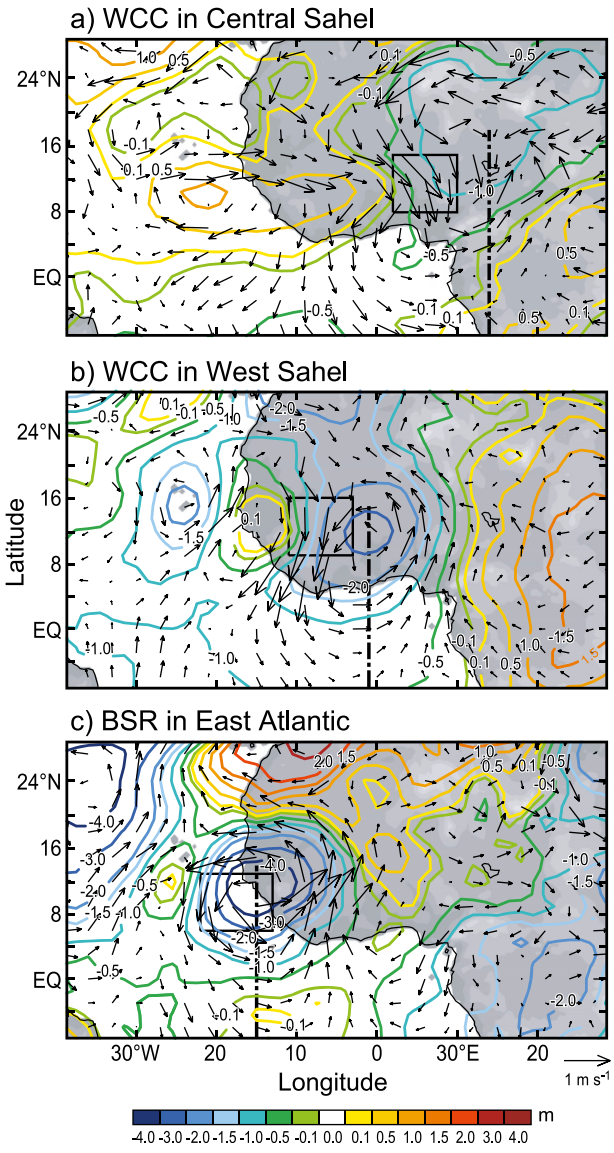

FIG. 5. Composites of ERA-Interim geopotential height (colored contour, m) and horizontal wind (vectors, m s^{-1}) anomalies at 700 hPa for the hourly times corresponding most closely to the time when TRMM observed (a) WCC in the central Sahel region, (b) WCC in the west Sahel region, and (c) BSR in the east Atlantic region. The black dashed line in each composite represents the approximate location of the AEW trough, and the box represents the region used for compositing.

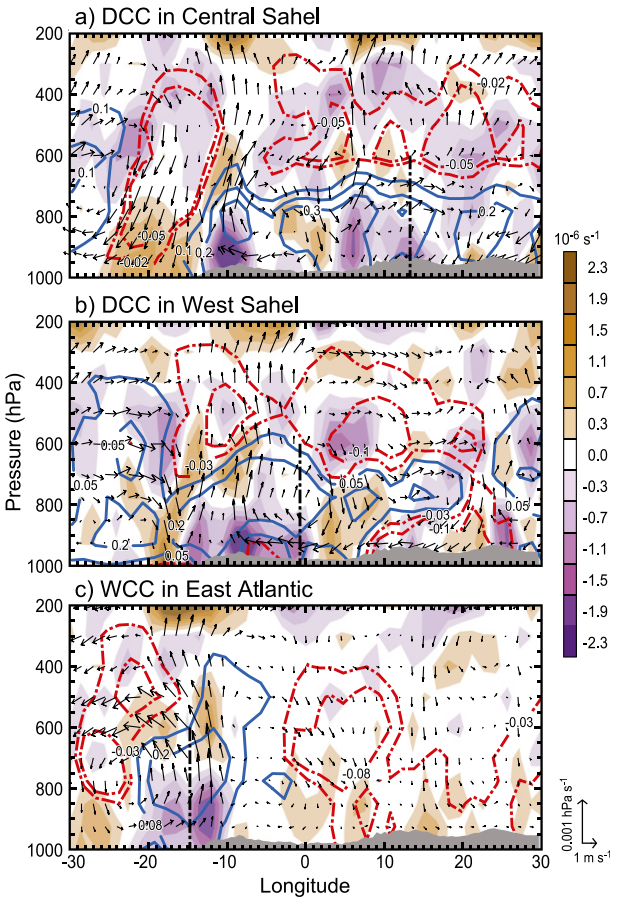

FIG. 6. Composite cross sections averaged over meridional bands bounded by (a) 8°–14°N, (b) 9°–15°N, and (c) 5°–12°N. The fields shown are ERA-Interim anomalies of divergence (shading, 10^{-6} s^{-1}), specific humidity (contours in g kg^{-1}, with solid blue lines indicating positive values and red negative), and air motion (vectors, scale at bottom) in the plane of the cross section for the hourly times corresponding most closely to when TRMM observed (a) DCC in central Sahel, (b) DCC in west Sahel, and (c) WCC over the east Atlantic region. Gray shading represents the average topographic relief in the given latitude belt.

are similar to Figs. 6a,b and, therefore, not shown. In each case, a moist low-level region with enhanced convergence and upward motion is observed to the west (ahead) of the approximate location of the trough axis. The zone of maximum frequency of DCC corresponds well to the synoptic-scale zone of upward motion associated with the AEWs. The wave itself appears to be a stretched version of convection (Mapes et al. 2006), with its upward motion region favoring the occurrence of smaller-scale and shorter-lived MCSs. We found a similar stretched relationship of DCC to equatorial waves over the Indian Ocean (Zuluaga and Houze 2013). The Saharan air layer (SAL) is a well-known midlevel feature over sub-Saharan Africa, and Figs. 6a,b show that those cases where DCC elements were observed over the African continent, the shallow moist layer is also overridden by relatively dry air aloft that likely inhibits deep convection except where the wave dynamics and lower-level moist monsoonal flow provide a sufficiently favorable environment to support convection breaking through the dry layer. In the composite for WCC over the east Atlantic region (Fig. 6c), intense vertical motion is observed with positive moisture anomalies reaching the middle troposphere. This situation, which also

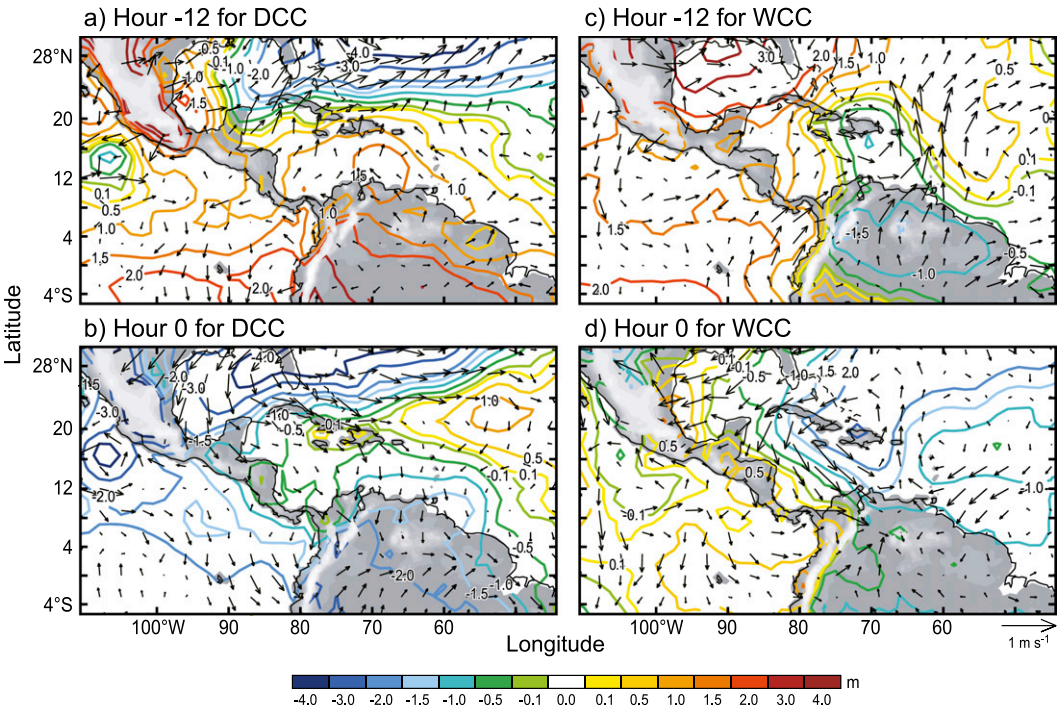

FIG. 7. Composites of ERA-Interim geopotential height (contour, m) and horizontal wind (vectors, m s^{-1}) anomalies at 850 hPa for (a) −12 and (b) 0 h from the time when DCC were observed in the northern Colombia region, and (c) −12 and (d) 0 h from the times when WCC were observed in the same region.

occurred when BSR were observed (not shown here) may partially be a result of slight orographic enhancement of lifting of the monsoon southwesterlies directing flow to the western side of the gentle slopes on the coast of West Africa in combination with the AEW trough passage.

b. Extreme convection in the equatorial America sector

1) DEEP AND WIDE CONVECTIVE CORES ON THE CARIBBEAN SIDE OF THE ANDES

Whereas much is known about the meteorology of equatorial Africa—dominated by the AEJ, AEWs and the southwest monsoon—there have been comparatively few studies of the factors governing convective events in the equatorial latitudes of the Americas. This region differs markedly from Africa at the same latitudes; the landmass is very narrow, contains high mountains, and is surrounded by oceans—in stark contrast to the presence of the vast dry Sahara that bounds all of the relatively flat equatorial Africa. Yet this region lies in the same equatorial belt, and some similar convective behaviors might be expected. We, therefore, use the same methodology as applied to Africa to elicit the similarities and differences of extreme convective phenomenology in the two regions.

The South American sector is divided by the Andes, with the extreme convection exhibiting different behaviors on the Pacific and Caribbean sides of the mountain range. In this section we examine the intense convection on the Caribbean side of the Andes in northern South America. Figures 7b,d show composites of wind and geopotential height anomalies averaged for hours that were close to the time when 84 DCC and 166 WCC were observed (0 h) over the northern Colombia region.

The DCC and WCC manifest strongly in the small inland area of northern Colombia that lies to the east and north of the Andes (Fig. 3b). On this Caribbean side of the Andes, the intense convection is centered in Colombia. The intense convection in this region is diurnally modulated where the DCC are strongly diurnally controlled. Figure 7a contains composites for 12 h before the times when DCC were observed. At this time, the anomaly fields show offshore flow across Colombia and Venezuela from the northern fringes of the Andes, consistent with the anomaly height gradient at this time. Positive 850-hPa height anomalies over most of northern South America had a southwest–northeast gradient, forcing the flow offshore and discouraging convective formation over the landmass. When the DCC were present (at 0 h, Fig. 7b), the anomaly height gradient favored onshore flow toward the mountains bounding

the inland inter-Andean valleys. This reversal in the atmospheric fields over a 12-h period produces convergence in the northern fringes of the Andes and forces the observed extreme convection to produce storms containing DCC to occur on the northeastern side of the mountains. That this change over the 12 h preceding DCC occurrence is associated with the diurnal heating cycle is confirmed by compositing maps of the 850-hPa geopotential height and wind fields at 6-hourly intervals for the same region and time period (not shown). The surface pressure and wind fields exhibit corresponding diurnal behavior. As we will show in section 6, all the DCC cases over this region tend to occur in the late afternoon, so that the zero hour in Fig. 7b is basically the composite map for that time of day. We will further examine the diurnal cycle in section 6.

In contrast to the situation for DCC, the factors controlling when the intense convection takes on mesoscale organization in the form of WCC are not purely diurnal. In addition to the diurnal forcing, synoptic conditions take on a distinct character when WCC occur on the Caribbean side of the northern Colombia region that is not seen when the DCC occur. A half-day before WCC occur (Fig. 7c), a region with anomalously low geopotential heights exists over the Caribbean island of Hispaniola, favoring an anomalous cyclonic circulation (such circulation is more evident on the 700-hPa level, not shown). Meanwhile, the South American continent has negative anomalies of geopotential height and diurnally forced offshore flow. By 0 h (Fig. 7d), the cyclonic circulation associated with the lower-than-average geopotential height has deepened and moved westward with enhanced anomalous flow now directed toward the South American continent from a deeper midlevel trough. This flow configuration favors low-level convergence in the inland valleys of the northern Andes foothills. The cyclonic circulation feature located over the Caribbean Sea thus produces the conditions favoring the occurrence of storms containing WCC over the foothills of the Andes ranges in northern South America. This synoptic-scale trough can be associated with easterly waves, which are commonly embedded in the climatological IALLJ flow in these latitudes (Amador 2008).

2) Wide convective cores and broad stratiform regions on the Pacific side of the Andes

Figure 8 shows composites of geopotential height and wind vector anomalies at 850 hPa calculated averaging the hours when TRMM detected 210 WCC and 55 BSR over the Colombian coast region (recall box in Fig. 1). In analyzing this region, we focus on the WCC and BSR since convective cores in this region do not reach DCC dimensions. The composite synoptic patterns at 850 hPa for the hour 0 of the WCC and BSR occurrence are shown in Figs. 8b,f, while other panels depict the anomaly patterns for times at various lags relative to the hour 0 of the two different forms of convection.

The pattern in Fig. 8a is the reanalysis composite for times 12 h before the occurrence of WCC in the Colombian coast region. It shows an anomalous low pressure center at 850 hPa. We saw in the preceding section that the 0-h synoptic pattern corresponding to WCC occurrence on the Caribbean side of the Andes exhibited an 850-hPa low-height anomaly that might have been associated with an easterly wave trough. The low anomaly in Fig. 8a and the other panels of Fig. 8 might also be associated with easterly wave troughs; however, the role of easterly waves cannot be determined from the present dataset. The circulation around the low anomaly at −12 h in Fig. 8a directs westerly wind toward and somewhat parallel to the Andes range. By 0 h, when WCC were in the Colombian coast box, the low pressure has deepened favoring an enhanced southwesterly jet parallel to the Pacific coast (Fig. 8b). This feature, known as the Chocó jet, directs strong flow from the Pacific along and toward the western Andes near the coast of Colombia. Also associated with this deepened vortex is a strengthening and recurving of the normally zonal wind associated with the IALLJ. This pattern is associated with anomalous low-level convergence on the Colombian coast and nearby Pacific Ocean region (not shown). Figure 9a shows a cross section of the composite data fields for the 0 h that extends west–east across the Colombian Pacific coastal Andes range. The reanalysis data show mean ascent over the windward slope of the mountains where they are intersected by the cross-barrier component of the Chocó jet. The occurrence of extreme convection in the form of WCC echoes coincides with the orographic forcing. Deep convective clouds have been widely observed to arise from the buoyant instability triggered and channeled by a forced cross-barrier flow that surmounts the terrain in areas with temperature and moisture stratification (Houze 2012). In the case of Fig. 9a the column of rising air is characterized by low-level convergence at the mountainside, upper-level divergence, negative anomalies of pressure velocity (i.e., enhanced upward motion), and positive anomalies of specific humidity. As time progresses to 6 h after the WCC are present (Fig. 8c), the low weakens, but the Chocó jet is stronger.

We now examine the synoptic-scale conditions associated with the occurrence of BSR echoes over near-coastal ocean on the west side of the Andes (i.e., when BSR were occurring in the box Colombian coast in

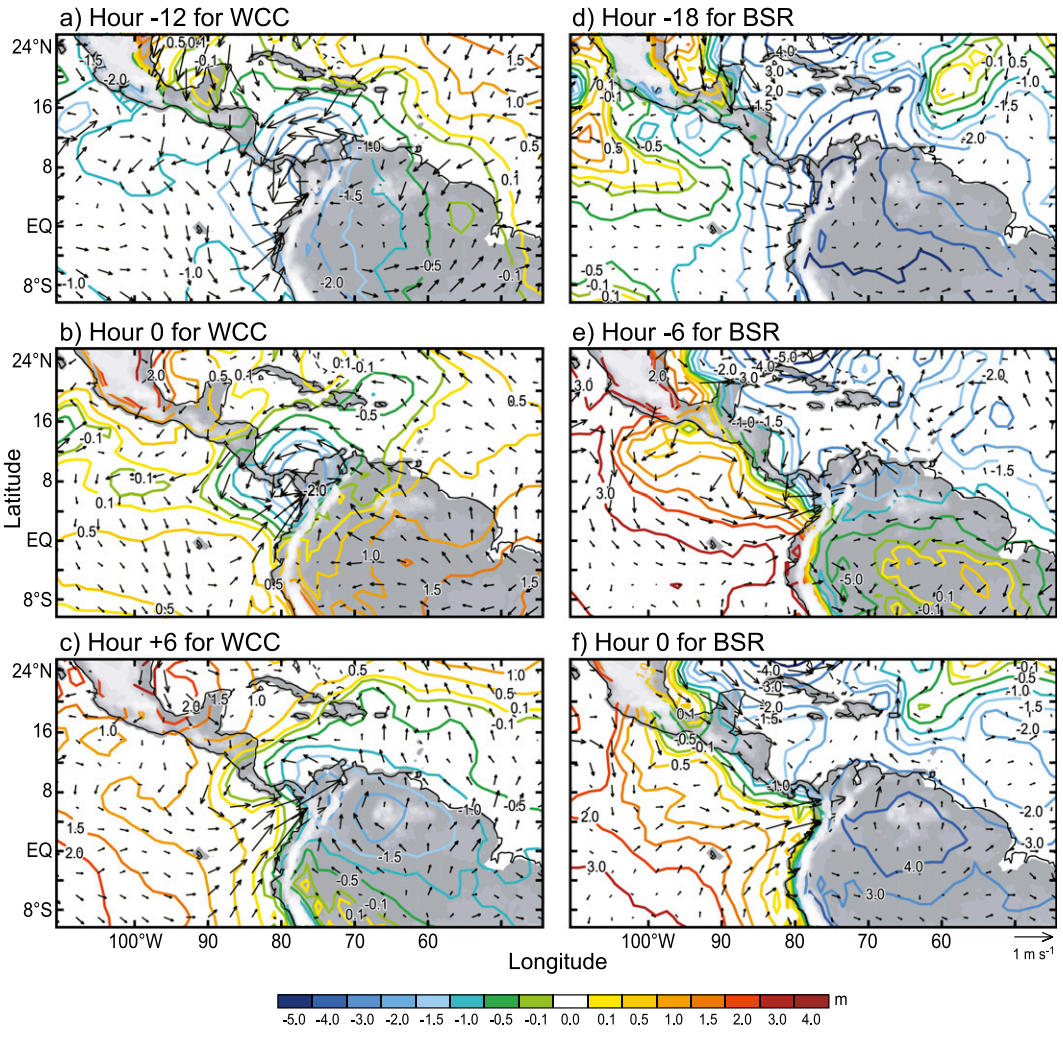

FIG. 8. Composites of ERA-Interim geopotential height (contour, m) and horizontal wind (vectors, m s^{-1}) anomalies at 850 hPa for (a) −12, (b) 0, and (c) +6 h from the times when WCC were observed in the Colombian coast region, and (d) −18, (e) −6, and (f) 0 h from the time where BSR were observed in the same region.

Fig. 1). The different panels of Fig. 8 are placed side by side because the left-hand panels have a rough similarity to the right-hand panels; that is, the synoptic patterns at −12, 0, and +6 h from the time of occurrence of WCC have a qualitative similarity to synoptic patterns at 18, −6, and 0 h from the time of occurrence of BSR echoes. These composite similarities strongly suggest that the BSR echoes identified in this region by TRMM are associated with MCSs similar to those in which WCC maximize 6 h earlier. In other words, the BSR echoes are markers of MCSs in similar environments but in a later stage of development than the MCSs containing WCC.

Figure 8f shows that when the BSR echoes occurred, the wind anomaly field at 850 hPa exhibited a strong Chocó jet at 850 hPa over the Pacific east of the Andes with a substantial cross-barrier flow component intersecting the mountain range. Strong low-level convergence of the synoptic-scale flow thus occurs along the windward slopes of the Andes. This composite flow pattern is like that seen 6 h after the WCC occurrences in this same region (Fig. 8c), consistent with the BSR echoes being a manifestation of the later states of MCSs in this region. That is, the 6-h time scale observed between composites in this region is an approximate time needed for the population of storms with WCC elements to become storms containing BSR. This time scale is similar to the time scale that was observed in the evolution of the convective cloud population over the equatorial Indian Ocean (Zuluaga and Houze 2013). Consistent with the southwesterly Chocó jet at these times was the existence of a negative height anomaly centered over northern South America.

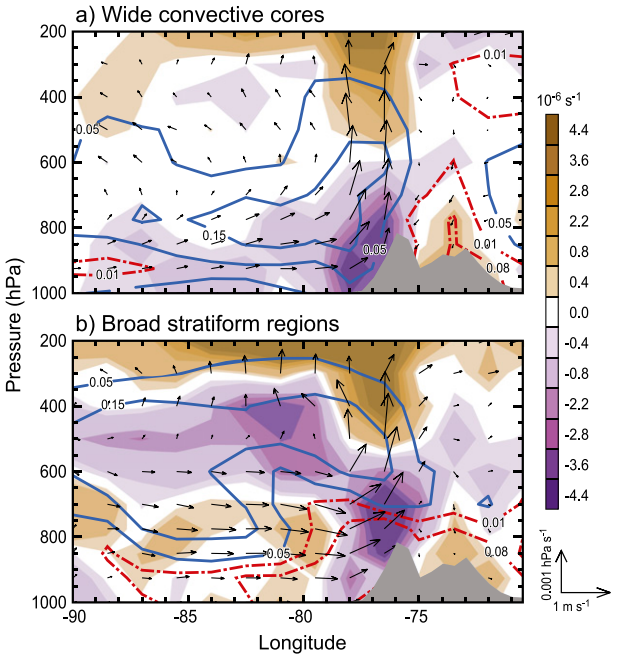

FIG. 9. Composite cross sections averaged over meridional bands bounded by 2°–8°N. The fields shown are ERA-Interim anomalies of divergence (shading, $10^{-6}\,s^{-1}$), specific humidity (contours in $g\,kg^{-1}$, with solid blue lines indicating positive values and red negative), and air motion (vectors, scale at bottom) in the plane of the cross section for the hourly times corresponding most closely to when TRMM observed (a) WCC and (b) BSR in the Colombian coast region. Gray shading represents the average topographic relief between 2° and 8°N.

Figures 9a,b show west–east vertical cross sections across the Andes and adjoining Pacific Ocean for the times that WCC and BSR echoes are maximum on the Pacific side of the Andes. These cross sections are for the same times of reanalysis data displayed in the plan view in Figs. 8b,f. These figures show that the anomaly mid- to low-level cross-barrier flow is somewhat stronger for the times of BSR echoes than at the times of WCC echoes. This difference could be related to the sampling by TRMM; however, heating feedback of the MCSs producing the echoes might also be producing a positive feedback that strengthens the cross-barrier flow as the MCSs mature. It is notable that at the time of the occurrence of BSR, the low-level atmosphere west of 78°W becomes divergent while the middle atmosphere becomes convergent with a layer of positive anomalies in specific humidity overlying negative anomalies of surface humidity (Fig. 9b). This pattern of midlevel convergence lying above a drier and divergent atmosphere corresponds to those situations of mature convective cells that develop well-defined stratiform precipitation regions (Zipser 1977; Houze 2004). This structure in the reanalysis composite is a further indication that the BSR occurrences correspond

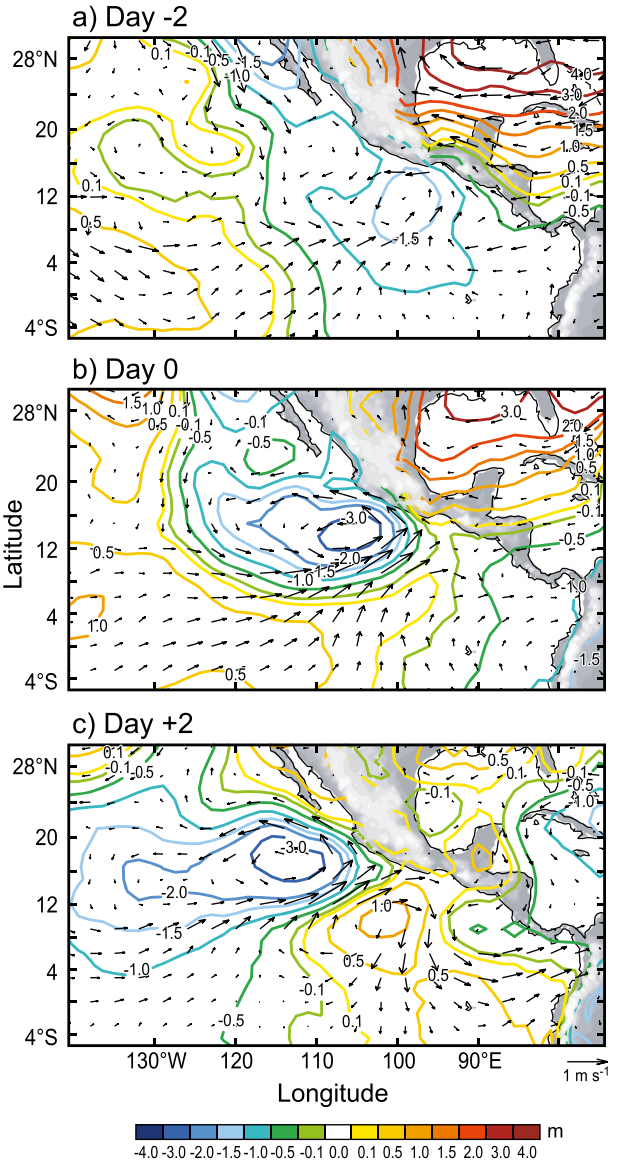

FIG. 10. Composites of ERA-Interim geopotential height (contour, m) and horizontal wind (vectors, m s^{-1}) anomalies at 850 hPa for (a) −2, (b) 0, and (c) +2 days of the time when TRMM detected BSR in the east Pacific region.

to later stages of MCS development in this region. The fact that this structure appears in the synoptic-scale reanalysis composite is an indication of feedback or synergistic cooperation among the synoptic-scale flow pattern, mesoscale system dynamics, and orography to maximize the occurrence of BSR in the region of the Pacific west of the Andes ridge.

c. *Broad stratiform regions in the east Pacific ITCZ*

Figure 10b shows composites of ERA-Interim geopotential height and wind vector anomalies at 850 hPa

calculated by averaging 167 days when BSR were observed by the TRMM PR (day 0) in the region of the east Pacific ITCZ (east Pacific box in Fig. 1). In addition, composites for 2 days before and after day 0 are presented in Figs. 10a,c. Figure 10a shows anomalously low geopotential heights and an associated weak cyclonic circulation centered off the Pacific coast of Mexico and Guatemala (~100°W, 10°E). As time progresses toward day 0 of the occurrence of BSR, the low geopotential height anomaly deepens, and the cyclonic circulation intensifies, with a characteristic low-level cross-equatorial flow that favors positive anomalies of surface moisture convergence (not shown) in the region where the BSR occur. By +2 day, the synoptic-scale cyclonic anomaly has moved farther northwest. This progression continues northwest paralleling the coastline of Central America with an approximate speed of 5° of longitude per day and is still appreciable up to 5 days after BSR were observed over the east Pacific region (not shown). This anomalous disturbance is probably related to westward-moving tropical waves (Nitta et al. 1985; Serra and Houze 2002). Such waves have a tendency to spawn tropical cyclones (e.g., Raymond et al. 1998; Rappaport and Mayfield 1992). Thus, MCSs with BSR echoes coincide with this regime of tropical easterly waves. We have determined that of the 167 BSR that we have identified in the east Pacific region, 30 BSR were associated with tropical depressions, 4 with tropical storms, and 6 with tropical cyclones. To reach this conclusion, we used the revised northeast and north-central Pacific hurricane best track data (HURDAT2) from the National Hurricane Center and the Joint Typhoon Warning Center (Landsea and Franklin 2013). The location of the centroid and time of occurrence of each BSR echo object was matched to any tropical storm track that occurred within 500 km and 24 h of the BSR. These are conservative and valid assumptions considering the limitation of the TRMM satellite, which samples a given location by using instantaneous snapshots widely separated in time, and that the cloud shield and precipitation associated with any tropical depression would cover spatial regions much greater than 500 km (e.g., Kummerow et al. 1998; Kelley et al. 2010).

A similar analysis to the one presented in Fig. 10 was done for days when WCC were observed in the east Pacific region; the composite maps obtained are similar to those for BSR and are, therefore, not shown. The characteristic low pressure center with cyclonic circulation that favors low-level convergence was observed, especially during day 0 when WCC were apparent. However, the northwestward progression of negative geopotential height anomalies was not as distinguishable as the one observed for when BSR occurred in the east Pacific region. Using the same HURDAT2 database, it was found that 14 out of 117 cases with WCC were associated with a tropical depression (10 WCC), tropical storm (2 WCC), or tropical cyclone (1 WCC).

6. Diurnal cycle of extreme echo events over the African and American sectors

Figure 11 shows the diurnal variation of the normalized frequency of occurrence of DCC, WCC, and BSR echoes in each of the regions indicated in Fig. 1. We applied a 4-h running mean to minimize sampling errors in diurnal calculations with TRMM data as suggested by Negri et al. (2002). The axes are in mean solar time (MST), which is the true local time. In the central and west Sahel, and northern Colombia regions the DCC echoes exhibit a strong late afternoon peak (1600–1800 MST, Figs. 11a,b,d). Several hours later, the WCC reach a peak in frequency, albeit a rather broad peak ranging across midnight, from about 2000 to about 0500 MST. The BSR echoes in those regions exhibit a clear peak in probability of occurrence in the morning hours (~0200–0700 MST in central Sahel, ~0600–0900 MST in west Sahel, and ~0200–0600 MST in northern Colombia). This sequence of peak probability of the three categories of extreme echo can be associated with developmental stages of MCSs, which are characterized by deep and more isolated cells in the early stages of MCS development, widening of convective cores to mesoscale dimension in intermediate stages, and large stratiform precipitation area formation in the mature to late stages of MCS life cycle. Although we are drawing these inferences from TRMM radar snapshots, we have confirmed from continuous ground-based radar data that in environments where MCSs are likely, the probabilities of the three echo forms follow the same sequence seen here (Zuluaga and Houze 2013).

The regions dominated by oceans generally do not exhibit DCC, defined as 40-dBZ echoes reaching 10-km height. Therefore, we use a 30-dBZ threshold in describing the diurnal cycle of storms containing DCC in the east Atlantic, the Colombian coast, and the east Pacific regions in Fig. 11. The oceanic regions exhibit a tendency for WCC echoes to be present most frequently in the early morning hours, around 0600 MST, with the maximum frequency of BSR echoes occurring several hours later, as expected, since they reflect a later stage of MCS development. The times of peak occurrence of WCC and BSR echoes are less distinct in the east Pacific, probably because of the strong synoptic forcing that occur in this region (section 5c).

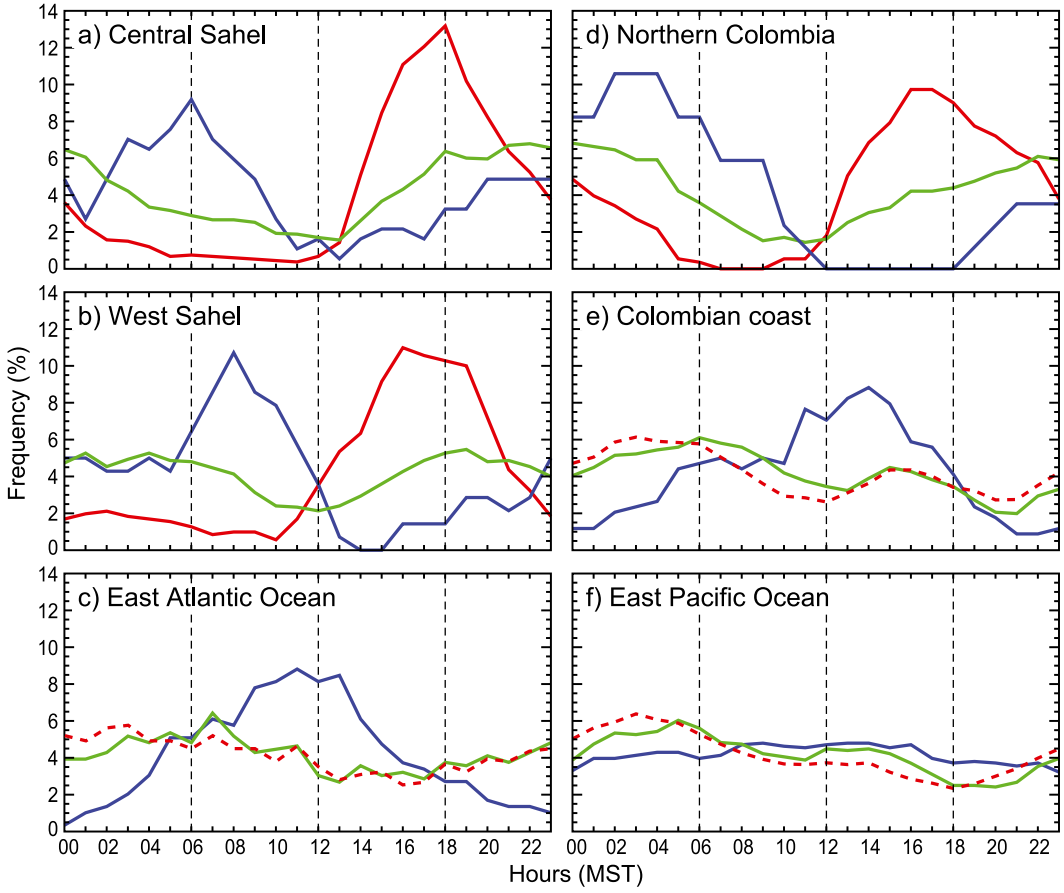

FIG. 11. (a)–(f) Diurnal cycle of the frequency of occurrence of DCC (red), WCC (green), and BSR (blue) in the indicated regions. Red dashed line in (c),(e), and (f) corresponds to the diurnal cycle for DCC using the 30-dBZ reflectivity threshold for oceanic regions.

7. Conclusions

This study analyzes the most extreme precipitation elements that occur in conjunction with convective storms in the near-equatorial band including Africa, the Americas, and the adjoining oceans (Atlantic, Caribbean, and Pacific). TRMM satellite PR data for the summer months (JJA) of 1998–2012 identify the convective elements. ECMWF ERA-Interim reanalysis data characterize the synoptic conditions around the time of occurrence of extreme echo elements. Regional analysis of three extreme echo categories shows how extreme convective events in this tropical belt occur in a wide variety of forms depending on topographic conditions, synoptic-scale dynamics, and the local diurnal cycle.

- The occurrence of storms containing DCC is highly probable over continental regions, especially those with significant topographical features, specifically in the northern ranges of the Andes in South America. Storms containing DCC are almost entirely convective, relatively small, intense, and significantly efficient in producing lightning flashes. They represent an early stage of MCS development. The vast savannas west of Sudan have a high probability of occurrence of storms with DCC. The deep convective elements in these regions are likely produced by strong updrafts made possible by strong low-level buoyancy maximized by diurnal daytime heating. They exhibit a pronounced late afternoon maximum in their frequency of occurrence.
- Storms containing WCC echoes, indicative of the aggregation of deep convective cells in middle stages of MCS development, maximize in the same locations as DCC, but they also occur over oceanic regions, in particular the Pacific coast of Colombia and Panama and the east Atlantic Ocean west off the coast of Africa. Being in an intermediate stage of MCS evolution, storms containing WCC have wider precipitation regions generally accounting for more rainfall than storms with DCC. Over sub-Saharan Africa, WCC echoes are associated with the troughs of easterly

waves. Over northern Colombia they are favored by low pressure systems at midlevels that might be associated with easterly waves. Over the Colombia–Panama coast they are enhanced by orographic uplift where the Chocó jet impinges on the Andes.

- Storms containing BSR echoes occur most frequently over the ocean off the coast of equatorial West Africa, over the east Pacific near the coasts of Colombia and Panama, and in the equatorial Pacific ITCZ. Representing a final and more mature state of MCSs, the storms with BSR contain high proportions of stratiform rain. Because of their large area they produce the highest rain accumulations but they exhibit a limited production of flash rates. The oceanic locations of storms with BSR have minimal diurnal variation in surface conditions, and warm moist boundary layers favoring the continual regeneration of convection throughout the day and night without strong disruption by the diurnal cycle. That is, the storms containing BSR have "sustainability" as hypothesized by Yuter and Houze (1998) and can, therefore, develop stratiform regions of large proportion. Along the South American west coast, orographic lifting where the Chocó jet encounters the Andes further enhances the storms with BSR. Off the Pacific coast of Central America, storms with BSR are associated with strong midlevel cyclonic vorticity and often develop into tropical cyclones.
- The diurnal frequencies of occurrence of DCC, WCC, and BSR exhibit systematic behavior, with DCC echoes preceding WCC by a few hours and WCC preceding BSR by several hours. Over land areas, the peak occurrence of DCC echoes is the most pronounced, favored by a strong solar heating cycle. However, over land nocturnal cooling of the boundary layer can truncate this life cycle preventing the storms to develop into large stratiform regions. In maritime and coastal areas all three stages are observed. Over purely oceanic zones, however, the DCC echoes are weaker and are better described by a threshold of 30 dBZ instead of 40 dBZ. The times between maximum frequencies of the three echo types are longer in regions with greater synoptic and/or orographic forcing.

Acknowledgments. This research was supported by National Aeronautics and Space Administration Grants NNX13AG71G and NNX10AH70G, National Science Foundation Grant AGS-1144105, and Department of Energy Grant DE-SC0008452. Thanks to K. Rasmussen who provided many insightful discussions and comments. Thanks also to three anonymous reviewers that contributed with helpful comments. Beth Tully provided graphics and editing support. ECMWF ERA-Interim data used in this study were obtained from the ECMWF data server. The TRMM dataset was accessed from the NASA GES DISC data center.

REFERENCES

Alory, G., C. Maes, T. Delcroix, N. Reul, and S. Illig, 2012: Seasonal dynamics of sea surface salinity off Panama: The far eastern Pacific fresh pool. *J. Geophys. Res.,* **117,** C04028, doi:10.1029/2011JC007802.

Amador, J. A., 2008: The Intra-Americas sea low-level jet overview and future research. *Ann. N. Y. Acad. Sci.,* **1146,** 153–188, doi:10.1196/annals.1446.012.

——, E. J. Alfaro, O. G. Lizano, and V. O. Magana, 2006: Atmospheric forcing of the eastern tropical Pacific: A review. *Prog. Oceanogr.,* **69,** 101–142, doi:10.1016/j.pocean.2006.03.007.

Aspliden, C. I., Y. Tourre, and J. B. Sabine, 1976: Some climatological aspects of West African disturbance lines during GATE. *Mon. Wea. Rev.,* **104,** 1029–1035, doi:10.1175/1520-0493(1976)104<1029:SCAOWA>2.0.CO;2.

Atlas, D., D. Rosenfeld, and D. A. Short, 1990: The estimation of convective rainfall by area integrals: 1. The theoretical and empirical basis. *J. Geophys. Res.,* **95,** 2153–2160, doi:10.1029/JD095iD03p02153.

Awaka, J., T. Iguchi, and K. Okamoto, 2009: TRMM PR standard algorithm 2A23 and its performance on bright band detection. *J. Meteor. Soc. Japan,* **87,** 31–52, doi:10.2151/jmsj.87A.31.

Barnes, H. C., and R. A. Houze Jr., 2013: The precipitating cloud population of the Madden–Julian oscillation over the Indian and west Pacific Oceans. *J. Geophys. Res. Atmos.,* **118,** 6996–7023, doi:10.1002/jgrd.50375.

Berrisford, P., D. Dee, K. Fielding, M. Fuentes, P. Kallberg, S. Kobayashi, and S. Uppala, 2009: The ERA-Interim archive. European Centre for Medium-Range Weather Forecasts Tech. Rep., ERA Rep. Series 1, Reading, United Kingdom, 16 pp.

Betts, A. K., R. W. Grover, and M. W. Moncrieff, 1976: Structure and motion of tropical squall-lines over Venezuela. *Quart. J. Roy. Meteor. Soc.,* **102,** 395–404, doi:10.1002/qj.49710243209.

Boccippio, D. J., S. J. Goodman, and S. Heckman, 2000: Regional differences in tropical lightning distributions. *J. Appl. Meteor.,* **39,** 2231–2248, doi:10.1175/1520-0450(2001)040<2231:RDITLD>2.0.CO;2.

Burpee, R. W., 1972: Origin and structure of easterly waves in lower troposphere of North Africa. *J. Atmos. Sci.,* **29,** 77–90, doi:10.1175/1520-0469(1972)029<0077:TOASOE>2.0.CO;2.

Carlson, T. N., 1969: Some remarks on African disturbances and their progress over tropical Atlantic. *Mon. Wea. Rev.,* **97,** 716–726, doi:10.1175/1520-0493(1969)097<0716:SROADA>2.3.CO;2.

Cecil, D. J., D. E. Buechler, and R. J. Blakeslee, 2014: Gridded lightning climatology from TRMM-LIS and OTD: Dataset description. *Atmos. Res.,* **135–136,** 404–414, doi:10.1016/j.atmosres.2012.06.028.

Cetrone, J., and R. A. Houze Jr., 2011: Leading and trailing anvil clouds of West African squall lines. *J. Atmos. Sci.,* **68,** 1114–1123, doi:10.1175/2011JAS3580.1.

Churchill, D. D., and R. A. Houze Jr., 1984: Development and structure of winter monsoon cloud clusters on 10 December 1978. *J. Atmos. Sci.,* **41,** 933–960, doi:10.1175/1520-0469(1984)041<0933:DASOWM>2.0.CO;2.

Cifelli, R., W. A. Petersen, L. D. Carey, S. A. Rutledge, and M. A. F. da Silva Dias, 2002: Radar observations of the kinematic, microphysical, and precipitation characteristics of two MCSs in TRMM LBA. *J. Geophys. Res.,* **107,** 8077, doi:10.1029/2000JD000264.

Fink, A. H., and A. Reiner, 2003: Spatiotemporal variability of the relation between African Easterly Waves and West African squall lines in 1998 and 1999. *J. Geophys. Res.,* **108,** 4332, doi:10.1029/2002JD002816.

Fortune, M., 1980: Properties of African squall lines inferred from time-lapse satellite imagery. *Mon. Wea. Rev.,* **108,** 153–168, doi:10.1175/1520-0493(1980)108<0153:POASLI>2.0.CO;2.

Futyan, J. M., and A. D. Del Genio, 2007: Deep convective system evolution over Africa and the tropical Atlantic. *J. Climate,* **20,** 5041–5060, doi:10.1175/JCLI4297.1.

Garstang, M., H. L. Massie Jr., J. B. Halverson, S. Greco, and J. Scala, 1994: Amazon coastal squall lines. Part I: Structure and kinematics. *Mon. Wea. Rev.,* **122,** 608–622, doi:10.1175/1520-0493(1994)122<0608:ACSLPI>2.0.CO;2.

Guy, N., and S. A. Rutledge, 2012: Regional comparison of West African convective characteristics: A TRMM-based climatology. *Quart. J. Roy. Meteor. Soc.,* **138,** 1179–1195, doi:10.1002/qj.1865.

Hamilton, R. A., and J. W. Archbold, 1945: Meteorology of Nigeria and adjacent territory. *Quart. J. Roy. Meteor. Soc.,* **71,** 231–264, doi:10.1002/qj.49707130905.

Hodges, K. I., and C. D. Thorncroft, 1997: Distribution and statistics of African mesoscale convective weather systems based on the ISCCP Meteosat imagery. *Mon. Wea. Rev.,* **125,** 2821–2837, doi:10.1175/1520-0493(1997)125<2821:DASOAM>2.0.CO;2.

Hou, A. Y., and Coauthors, 2014: The Global Precipitation Measurement Mission. *Bull. Amer. Meteor. Soc.,* **95,** 701–722, doi:10.1175/BAMS-D-13-00164.1.

Houze, R. A., Jr., 1977: Structure and dynamics of a tropical squall-line system. *Mon. Wea. Rev.,* **105,** 1540–1567, doi:10.1175/1520-0493(1977)105<1540:SADOAT>2.0.CO;2.

——, 1993: *Cloud Dynamics.* Academic Press, 573 pp.

——, 1997: Stratiform precipitation in regions of convection: A meteorological paradox? *Bull. Amer. Meteor. Soc.,* **78,** 2179–2196, doi:10.1175/1520-0477(1997)078<2179:SPIROC>2.0.CO;2.

——, 2004: Mesoscale convective systems. *Rev. Geophys.,* **42,** RG4003, doi:10.1029/2004RG000150.

——, 2012: Orographic effects on precipitating clouds. *Rev. Geophys.,* **50,** RG1001, doi:10.1029/2011RG000365.

——, and A. K. Betts, 1981: Convection in GATE. *Rev. Geophys.,* **19,** 541–576, doi:10.1029/RG019i004p00541.

——, D. C. Wilton, and B. F. Smull, 2007: Monsoon convection in the Himalayan region as seen by the TRMM Precipitation Radar. *Quart. J. Roy. Meteor. Soc.,* **133,** 1389–1411, doi:10.1002/qj.106.

——, K. L. Rasmussen, S. Medina, S. R. Brodzik, and U. Romatschke, 2011: Anomalous atmospheric events leading to the summer 2010 floods in Pakistan. *Bull. Amer. Meteor. Soc.,* **92,** 291–298, doi:10.1175/2010BAMS3173.1.

Iguchi, T., T. Kozu, R. Meneghini, J. Awaka, and K. Okamoto, 2000: Rain-profiling algorithm for the TRMM precipitation radar. *J. Appl. Meteor.,* **39,** 2038–2052, doi:10.1175/1520-0450(2001)040<2038:RPAFTT>2.0.CO;2.

——, ——, J. Kwiatkowski, R. Meneghini, J. Awaka, and K. Okamoto, 2009: Uncertainties in the rain profiling algorithm for the TRMM precipitation radar. *J. Meteor. Soc. Japan,* **87,** 1–30, doi:10.2151/jmsj.87A.1.

Kelley, O. A., J. Stout, M. Summers, and E. J. Zipser, 2010: Do the tallest convective cells over the tropical ocean have slow updrafts? *Mon. Wea. Rev.,* **138,** 1651–1672, doi:10.1175/2009MWR3030.1.

Kummerow, C., W. Barnes, T. Kozu, J. Shiue, and J. Simpson, 1998: The Tropical Rainfall Measuring Mission (TRMM) sensor package. *J. Atmos. Oceanic Technol.,* **15,** 809–817, doi:10.1175/1520-0426(1998)015<0809:TTRMMT>2.0.CO;2.

——, and Coauthors, 2000: The status of the Tropical Rainfall Measuring Mission (TRMM) after two years in orbit. *J. Appl. Meteor.,* **39,** 1965–1982, doi:10.1175/1520-0450(2001)040<1965:TSOTTR>2.0.CO;2.

Laing, A. G., and J. M. Fritsch, 1993: Mesoscale convective complexes in Africa. *Mon. Wea. Rev.,* **121,** 2254–2263, doi:10.1175/1520-0493(1993)121<2254:MCCIA>2.0.CO;2.

——, and ——, 1997: The global population of mesoscale convective complexes. *Quart. J. Roy. Meteor. Soc.,* **123,** 389–405, doi:10.1002/qj.49712353807.

Landsea, C. W., and J. L. Franklin, 2013: Atlantic hurricane database uncertainty and presentation of a new database format. *Mon. Wea. Rev.,* **141,** 3576–3592, doi:10.1175/MWR-D-12-00254.1.

Liu, C. T., E. J. Zipser, D. J. Cecil, S. W. Nesbitt, and S. Sherwood, 2008: A cloud and precipitation feature database from nine years of TRMM observations. *J. Appl. Meteor. Climatol.,* **47,** 2712–2728, doi:10.1175/2008JAMC1890.1.

Mapes, B. E., T. T. Warner, M. Xu, and A. J. Negri, 2003: Diurnal patterns of rainfall in northwestern South America. Part I: Observations and context. *Mon. Wea. Rev.,* **131,** 799–812, doi:10.1175/1520-0493(2003)131<0799:DPORIN>2.0.CO;2.

——, S. Tulich, J.-L. Lin, and P. Zuidema, 2006: The mesoscale convection life cycle: Building block or prototype for large-scale tropical waves? *Dyn. Atmos. Oceans,* **42,** 3–29, doi:10.1016/j.dynatmoce.2006.03.003.

Medina, S., R. A. Houze Jr., A. Kumar, and D. Niyogi, 2010: Summer monsoon convection in the Himalayan region: Terrain and land cover effects. *Quart. J. Roy. Meteor. Soc.,* **136,** 593–616, doi:10.1002/qj.601.

Moncrieff, M. W., 1992: Organized convective systems: Archetypal dynamical models, mass and momentum flux theory, and parametrization. *Quart. J. Roy. Meteor. Soc.,* **118,** 819–850, doi:10.1002/qj.49711850703.

Negri, A. J., T. L. Bell, and L. Xu, 2002: Sampling of the diurnal cycle of precipitation using TRMM. *J. Atmos. Oceanic Technol.,* **19,** 1333–1344, doi:10.1175/1520-0426(2002)019<1333:SOTDCO>2.0.CO;2.

Nesbitt, S. W., E. J. Zipser, and D. J. Cecil, 2000: A census of precipitation features in the Tropics using TRMM: Radar, ice scattering, and lightning observations. *J. Climate,* **13,** 4087–4106, doi:10.1175/1520-0442(2000)013<4087:ACOPFI>2.0.CO;2.

Nitta, T., Y. Nakagomi, Y. Suzuki, N. Hasegawa, and A. Kadokura, 1985: Global analysis of the lower tropospheric disturbances in the tropics during the northern summer of the FGGE year: 1. Global features of the disturbances. *J. Meteor. Soc. Japan,* **63,** 1–19.

Payne, S. W., and M. M. McGarry, 1977: The relationship of satellite inferred convective activity to easterly waves over West Africa and adjacent ocean during phase III of GATE. *Mon. Wea. Rev.,* **105,** 413–420, doi:10.1175/1520-0493(1977)105<0413:TROSIC>2.0.CO;2.

Poveda, G., and O. J. Mesa, 2000: On the existence of Lloró (the rainiest locality on earth): Enhanced ocean-land-atmosphere interaction by a low-level jet. *Geophys. Res. Lett.,* **27,** 1675–1678, doi:10.1029/1999GL006091.

——, P. R. Waylen, and R. S. Pulwarty, 2006: Annual and inter-annual variability of the present climate in northern South America and southern Mesoamerica. *Palaeogeogr.*

Palaeoclimatol. Palaeoecol., **234,** 3–27, doi:10.1016/j.palaeo.2005.10.031.

Powell, S. W., R. A. Houze Jr., A. Kumar, and S. A. McFarlane, 2012: Comparison of simulated and observed continental tropical anvil clouds and their radiative heating profiles. *J. Atmos. Sci.,* **69,** 2662–2681, doi:10.1175/JAS-D-11-0251.1.

Rappaport, E. N., and M. Mayfield, 1992: Eastern North Pacific hurricane season of 1991. *Mon. Wea. Rev.,* **120,** 2697–2708, doi:10.1175/1520-0493(1992)120<2697:ENPHSO>2.0.CO;2.

Rasmussen, K. L., and R. A. Houze Jr., 2011: Orogenic convection in subtropical South America as seen by the TRMM satellite. *Mon. Wea. Rev.,* **139,** 2399–2420, doi:10.1175/MWR-D-10-05006.1.

——, A. J. Hill, V. E. Toma, M. D. Zuluaga, P. J. Webster, and R. A. Houze Jr., 2014: Multiscale analysis of three consecutive years of anomalous flooding in Pakistan. *Quart. J. Roy. Meteor. Soc.,* doi:10.1002/qj.2433, in press.

Raymond, D. J., C. Lopez-Carrillo, and L. L. Cavazos, 1998: Case-studies of developing east Pacific easterly waves. *Quart. J. Roy. Meteor. Soc.,* **124,** 2005–2034, doi:10.1002/qj.49712455011.

Reed, R. J., and K. D. Jaffe, 1981: Diurnal variation of summer convection over west Africa and the tropical eastern Atlantic during 1974 and 1978. *Mon. Wea. Rev.,* **109,** 2527–2534, doi:10.1175/1520-0493(1981)109<2527:DVOSCO>2.0.CO;2.

——, D. C. Norquist, and E. E. Recker, 1977: Structure and properties of African wave disturbances as observed during phase III of GATE. *Mon. Wea. Rev.,* **105,** 317–333, doi:10.1175/1520-0493(1977)105<0317:TSAPOA>2.0.CO;2.

Romatschke, U., and R. A. Houze Jr., 2010: Extreme summer convection in South America. *J. Climate,* **23,** 3761–3791, doi:10.1175/2010JCLI3465.1.

——, S. Medina, and R. A. Houze Jr., 2010: Regional, seasonal, and diurnal variations of extreme convection in the South Asian region. *J. Climate,* **23,** 419–439, doi:10.1175/2009JCLI3140.1.

Rowell, D. P., and J. R. Milford, 1993: On the generation of African squall lines. *J. Climate,* **6,** 1181–1193, doi:10.1175/1520-0442(1993)006<1181:OTGOAS>2.0.CO;2.

Schumacher, C., and R. A. Houze Jr., 2003: Stratiform rain in the tropics as seen by the TRMM precipitation radar. *J. Climate,* **16,** 1739–1756, doi:10.1175/1520-0442(2003)016<1739:SRITTA>2.0.CO;2.

——, and ——, 2006: Stratiform precipitation production over sub-Saharan Africa and the tropical East Atlantic as observed by TRMM. *Quart. J. Roy. Meteor. Soc.,* **132,** 2235–2255, doi:10.1256/qj.05.121.

Serra, Y. L., and R. A. Houze Jr., 2002: Observations of variability on synoptic timescales in the East Pacific ITCZ. *J. Atmos. Sci.,* **59,** 1723–1743, doi:10.1175/1520-0469(2002)059<1723:OOVOST>2.0.CO;2.

Simpson, J., R. F. Adler, and G. R. North, 1988: A proposed Tropical Rainfall Measuring Mission (TRMM) satellite. *Bull. Amer. Meteor. Soc.,* **69,** 278–295, doi:10.1175/1520-0477(1988)069<0278:APTRMM>2.0.CO;2.

Smull, B. F., and R. A. Houze Jr., 1987: Rear inflow in squall lines with trailing stratiform precipitation. *Mon. Wea. Rev.,* **115,** 2869–2889, doi:10.1175/1520-0493(1987)115<2869:RIISLW>2.0.CO;2.

Steiner, M., R. A. Houze Jr., and S. E. Yuter, 1995: Climatological characterization of 3-dimensional storm structure from operational radar and rain-gauge data. *J. Appl. Meteor.,* **34,** 1978–2007, doi:10.1175/1520-0450(1995)034<1978:CCOTDS>2.0.CO;2.

Thorncroft, C., and M. Blackburn, 1999: Maintenance of the African easterly jet. *Quart. J. Roy. Meteor. Soc.,* **125,** 763–786, doi:10.1002/qj.49712555502.

——, and K. Hodges, 2001: African easterly wave variability and its relationship to Atlantic tropical cyclone activity. *J. Climate,* **14,** 1166–1179, doi:10.1175/1520-0442(2001)014<1166:AEWVAI>2.0.CO;2.

Velasco, I., and J. M. Fritsch, 1987: Mesoscale convective complexes in the Americas. *J. Geophys. Res.,* **92,** 9591–9613, doi:10.1029/JD092iD08p09591.

Yuan, J. A., and R. A. Houze Jr., 2010: Global variability of mesoscale convective system anvil structure from A-Train satellite data. *J. Climate,* **23,** 5864–5888, doi:10.1175/2010JCLI3671.1.

Yuter, S. E., and R. A. Houze Jr., 1998: The natural variability of precipitating clouds over the western Pacific warm pool. *Quart. J. Roy. Meteor. Soc.,* **124,** 53–99, doi:10.1002/qj.49712454504.

Zipser, E. J., 1977: Mesoscale and convective-scale downdrafts as distinct components of squall-line structure. *Mon. Wea. Rev.,* **105,** 1568–1589, doi:10.1175/1520-0493(1977)105<1568:MACDAD>2.0.CO;2.

——, C. T. Liu, D. J. Cecil, S. W. Nesbitt, and D. P. Yorty, 2006: Where are the most intense thunderstorms on Earth? *Bull. Amer. Meteor. Soc.,* **87,** 1057–1071, doi:10.1175/BAMS-87-8-1057.

Zuluaga, M. D., and G. Poveda, 2004: Diagnóstico de sistemas convectivos de mesoescala sobre Colombia y el océano Pacífico oriental durante 1998-2002 (Diagnostics of mesoscale convective systems over Colombia and the east Pacific Ocean during 1998-2002). *Av. Recur. Hidrául.,* **11,** 145–160.

——, and R. A. Houze Jr., 2013: Evolution of the population of precipitating convective systems over the equatorial Indian Ocean in active phases of the Madden–Julian oscillation. *J. Atmos. Sci.,* **70,** 2713–2725, doi:10.1175/JAS-D-12-0311.1.